



Kent Academic Repository

Smith, Michael D. and Richards, Carl (2023) *The influence of mach number and over-pressure on the structure of supersonic gas jets*. *Monthly Notices of the Royal Astronomical Society*, 526 (3). pp. 3407-3420. ISSN 0035-8711.

Downloaded from

<https://kar.kent.ac.uk/102957/> The University of Kent's Academic Repository KAR

The version of record is available from

<https://doi.org/10.1093/mnras/stad2879>

This document version

Publisher pdf

DOI for this version

Licence for this version

CC BY (Attribution)

Additional information

Versions of research works

Versions of Record

If this version is the version of record, it is the same as the published version available on the publisher's web site. Cite as the published version.

Author Accepted Manuscripts

If this document is identified as the Author Accepted Manuscript it is the version after peer review but before type setting, copy editing or publisher branding. Cite as Surname, Initial. (Year) 'Title of article'. To be published in **Title of Journal**, Volume and issue numbers [peer-reviewed accepted version]. Available at: DOI or URL (Accessed: date).

Enquiries

If you have questions about this document contact ResearchSupport@kent.ac.uk. Please include the URL of the record in KAR. If you believe that your, or a third party's rights have been compromised through this document please see our [Take Down policy](https://www.kent.ac.uk/guides/kar-the-kent-academic-repository#policies) (available from <https://www.kent.ac.uk/guides/kar-the-kent-academic-repository#policies>).

The influence of Mach number and overpressure on the structure of supersonic gas jets

Michael D. Smith[★] and Carl Richards

Centre for Astrophysics & Planetary Science, The University of Kent, Canterbury, Kent CT2 7NH, UK

Accepted 2023 September 18. Received 2023 September 18; in original form 2023 July 21

ABSTRACT

The Mach number is the primary parameter in determining the intrinsic driving properties, and effect on the environment of a supersonic jet. In the most basic form, a jet is released when a wall of a large high-pressure gas reservoir is punctured. The resulting high-pressure jet contains a configuration of shocks that continue to disturb the environment after the initial bow shock has passed. Here, we perform numerical simulations to determine the properties attributable to pure adiabatic hydrodynamic effects, taking a uniform stream out of a circular nozzle. We take a range of Mach numbers that, along with the jet overpressure, determine the flow pattern and shock locations. We distinguish conditions that generate Mach shock discs rather than a diamond pattern of oblique regular reflections. Potential observational diagnostics explored include the disc size, the distance from the nozzle, and oscillations in shock positions. Rapid oscillations occur in the divergent–convergent pattern through a feedback/hysteresis effect promoted by the ambient medium. The underlying flow patterns are independent of relative jet density, but heavy jets display both lower amplitude and lower frequency oscillations. We also study the energy transferred into the environment. Overpressured jets may contribute to noise and sound wave generation through screeching. However, these oscillations in the near-field are not sufficiently significant to regulate star and galaxy formation. We expect that upcoming high dynamic range and resolution observations will increasingly detect the shock patterns as jet gas transits from protostellar and galactic cores.

Key words: hydrodynamics – stars: jets – ISM: jets and outflows – galaxies: jets.

1 INTRODUCTION

A supersonic jet emerges when gas escapes from a puncture in the wall of a large high-pressure reservoir. As the pressure adjusts to the ambient pressure, a hydrodynamic flow generates a shock pattern that depends primarily on the degree of overpressure and the Mach number (e.g. Franquet et al. 2015).

This basic scenario for producing a collimated outflow has been argued as relevant to various degrees to those emanating from many astrophysical objects and Solar system bodies (e.g. Yelle, Soderblom & Jokipii 2004; Perucho & Martí 2007; White et al. 2014; Velović et al. 2022). This also applies to rocket engines, geysers, volcanic eruptions, hydrogen fuel injection, and champagne de-corking as reviewed by Smith & Keogh (2022, hereafter SK22).

An interpretation would constrain the jet properties such as the Mach number, density, and overpressure. In SK22, we achieved this by fixing the Mach number and exploring quantitatively how the density and overpressure fix the location of the shocks in the downstream flow. For low overpressures, a series of oblique crossing shocks occur, whereas for high overpressures, the oblique shocks are interrupted by a disc-shaped shock termed a Mach disc, which is followed by a disordered plume. Between the two extremes, we can

recognize cases where the Mach disc is small and repeated shocks still occur downstream, and where a prominent sheath is sustained until the flow breaks up. Each of these four flow patterns, illustrated in Fig. 1, could possess distinct detectable features.

A note on terminology is useful. The repeating structure termed regular reflection is often referred to as a diamond shock pattern. When a Mach disc is present, the flow is referred to as Mach reflection. In this case, an incident shock meets and reflects off the Mach disc above the axis. In a plane-parallel flow, we would use the terms Mach stem and triple point.

The structure of observed emission knots can then be interpreted in terms of the jet overpressure and other nozzle parameters. For example, Mach discs would also provide the strong shocks that may account for the X-ray emission from accreting young stars (Schneider, Günther & Schmitt 2011). To make progress, we determine here the conditions that generate Mach shock discs rather than a regular reflection pattern of oblique shocks.

We expect that the Mach number, M_{jet} , will be a crucial variable for two reasons. Firstly, a higher speed will stretch out the shock pattern as shown in many works as summarized by the Franquet et al. (2015) review. This includes the angle at which sound waves can propagate across the jet with $\theta = \sin^{-1} M_{\text{jet}}$. Secondly, as explored here, a threshold Mach number is expected beyond which separates the appearance of Mach shock discs from regular reflection. Thus, the conspicuous Mach discs appear only for a specific range of high

[★] E-mail: m.d.smith@kent.ac.uk

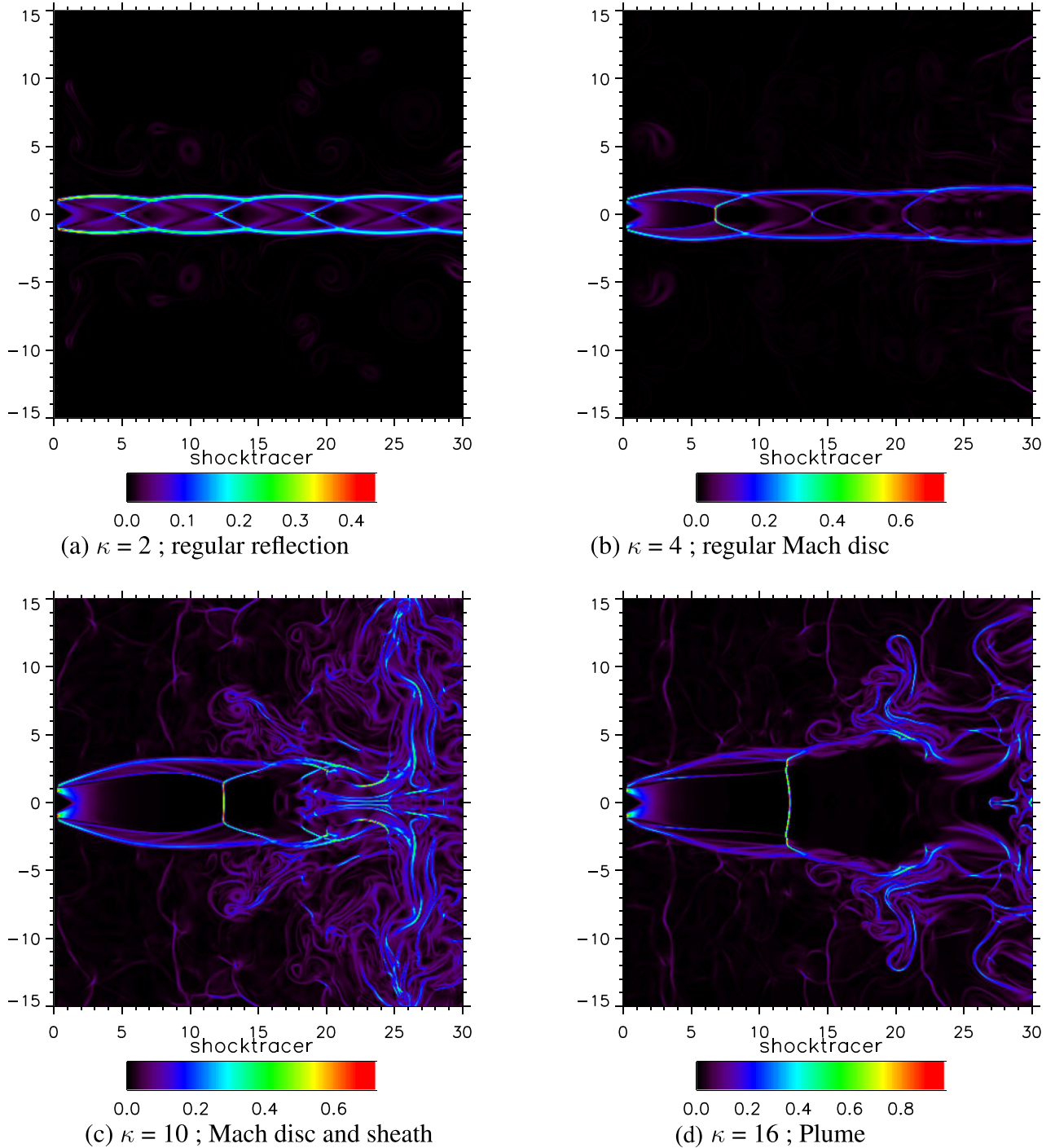


Figure 1. Illustrations of four distinct flow patterns in overpressured jets. These are cross-sections that capture locally high-pressure gradients and combine with interface recognition, adapted for display purposes. Common parameters to all panels are Mach number $M_{\text{jet}} = v_{\text{jet}}/c_{\text{jet}} = 2$, density ratio $\eta = \rho_{\text{jet}}/\rho_{\text{amb}} = 0.1$, and time $200R_{\text{jet}}/c_{\text{amb}}$.

overpressures and low Mach numbers. For high Mach numbers, hot shear layers are highlighted, and the influence of outflow boundary conditions is crucial.

Several simplifications are made here: the injected jet is uniform and circular with constant density and speed, the gas is adiabatic with specific heat ratio of $5/3$, and the jet begins as perfectly collimated. Cooling, chemistry, magnetic fields, gravity, and relativistic speeds were not included. Hence, additional physics as well as dynamics,

such as pulses, bursts, spray, precession, and shear, should be considered. This has been achieved in many sets of simulations for jets injected at the ambient pressure but remains to be systematically explored in the overpressured case.

To facilitate a comparison, we establish a set of diagnostics. This includes the position and shape of the shock fronts. We can then determine the degree of expansion and recollimation, and the onset of sustained oscillations in the overall pattern.

Simulations of jet propagation have delivered a means to understand the flows without the interference of laboratory instruments. Moreover, by exploring the initial and boundary conditions, we can probe inside the engine that drives the jet, whether from rockets, planetary vents, or astrophysical compact objects. This has led to a proliferation of studies that analyse the propagating jet on exit and attempt to work backwards to deduce the mechanism and processes within (e.g. Blackman & Lebedev 2022), as reviewed by Bally (2007), Smith (2012), and Martí (2019).

It should be noted that high Reynolds numbers are associated with the initial escape of the gas. That means that viscous effects are confined to a narrow boundary layer separating the jet from the ambient medium. Apart from this interface, the flow is inviscid. Hence, numerical simulations are valid for inviscid jets where the interface approximates to a tangential discontinuity across which the thermal pressure is constant.

Besides the origin of the jet, we are interested in how it interacts with the environment to provide positive or negative feedback that could be ultimately related to many evolutionary scenarios involving regulation and triggering (Rawlings & Jarvis 2004; Hillel, Schreier & Soker 2022). We therefore wish to determine how much energy continues to be poured into the surroundings in the form of noise, turbulence, and heat.

Smith & Keogh (2022) completed an analysis for Mach 2 jets that establish the basis for this work. We tested high numerical resolutions before settling on a standard that we work with below. We can summarize SK22 as follows:

(i) High-density jets generate quite steady channels and shock patterns with slow oscillations. Light jets also settle down except for high overpressures that oscillate with high amplitude.

(ii) Two extremes to the flow patterns were discussed. At low overpressures, a diamond shock pattern that involves intersecting oblique shocks occurs. At high overpressures, a normal Mach shock disc intercepts the oblique shocks at a triple point (a circle) due to the wide divergent–convergent structure.

(iii) At intermediate overpressures, a series of Mach shock discs can occur downstream of the stand-off shock, while at high overpressures a turbulent plume is predicted.

(iv) The oscillations drive sound waves into the ambient medium. A lateral dispersion of energy occurs in some cases. However, a major effect of this sloshing is to promote the advection of ambient gas away from the nozzle and draw more material towards the jet axis.

Here, we explore the shock configuration and stability at high Mach numbers. Note that we again assume cylindrical symmetry that may be realized in the near-field of a circular nozzle but not the far-field within the turbulent plume. We also assume both media are ideal gases and use an adiabatic equation of state. We thus only determine here the properties attributable to pure non-relativistic hydrodynamics.

Hypersonic Mach numbers were studied by Belan et al. (2013), utilizing and comparing laboratory and numerical experiments. These were for pressure-matched jets, both density-matched and heavy. They demonstrated the accuracy of the PLUTO code.

Jet simulations were performed with the same set-up but in full three dimensions by Donohoe & Smith (2016). However, these were pressure-matched jets and so displayed little internal shock structure near the nozzle. In addition, these simulations could only be run to a time of less than 10 units as defined by the jet radius and ambient sound speed. The time unit is $R_{\text{jet}}/c_{\text{amb}}$, where the time-step is measured by the jet radius R_{jet} and ambient sound speed c_{amb} . In

Table 1. Physical and grid dimensions in cylindrical coordinates (R , Z). For low-density Mach 8 simulations, larger physical sizes were found to be necessary.

Mach number	Physical size in R_{jet}	Uniform section in R_{jet}	Total zones	Uniform zones
2	65×130	15×30	300×600	200×400
4	65×160	15×60	300×1000	200×800
6	65×190	15×90	300×1400	200×1200
8, $\eta = 10$	65×220	15×120	300×1800	200×1600
8, $\eta = 0.1$	130×440	30×2400	600×3600	400×3200

contrast, we run these two-dimensional simulations to 200 time units. This aided our interpretation of radio galaxies (Smith & Donohoe 2019) and associated X-ray cavities (Smith & Donohoe 2021) during the initial escape from a galaxy and propagation into the intergalactic medium.

By limiting the analysis to the near-field, we can justify the two-dimensional approach that is consistent with laboratory experiments and simulations, and which can be directly compared (Belan et al. 2013, 2014). This allows us to perform simulations over extremely long durations. In this paper, we run simulations to 200 time-steps as given by the jet radius and ambient sound speed. We follow only the region near the nozzle where a steady flow pattern may be established after the initial impulse has vacated the entire computational domain. This near-field region must be sufficiently long and wide so as to incorporate the internal shocks, while the complete computational domain includes the flow cocoon and pressure regulation from an extended ambient reservoir.

2 METHOD

2.1 The code and boundary conditions

The simulations were performed in two dimensions with axial symmetry using PLUTO, a grid-based code, incorporating Godunov-type shock-capturing schemes. The code is freely distributed (Mignone et al. 2007).¹ After comparing the results of numerous options, we chose a fast linear interpolation time-stepping Riemann solver (denoted HLLC) as developed by Harten, Lax, and Van Leer and detailed by Toro, Spruce & Speares (1994). The Hancock time-stepping Courant–Friedrichs–Lewy factor is taken as 0.4 to ensure numerical stability.

The equations of compressional hydrodynamics of ideal gases are evolved. Two-dimensional axial symmetry is taken with radial and axial velocity components. The flow enters from a circular hole in a wall. The other boundaries are free outflow as is always taken for jet and radio galaxy simulations to avoid reflection of sound and shock waves.

The computational domain is covered by a fixed grid with a main uniform section plus a very extended staggered grid outside. The length of the uniform section is set to be proportional to the Mach number. In detail, the main set of simulations was performed on uniform cylindrical grids of 200 radially distributed zones and $200 \times M_{\text{jet}}$ along the axis. This converts into $15R_{\text{jet}}$ and $15M_{\text{jet}}R_{\text{jet}}$, respectively. Hence, the length of the grid is proportional to the Mach number, anticipating that the flow pattern will be stretched to some extent. The grid parameters are summarized in Table 1.

¹<http://plutocode.ph.unito.it/>

In addition, a vast reservoir is required to allow the pressure disturbances to freely propagate outwards without being influenced by the domain boundary. Extended regions of staggered zones of number 100×200 were added in the radial and axial directions to take the full grid to $(65 \times 100 + 15M_{\text{jet}})R_{\text{jet}}$. This was checked and found to be inadequate for the low-density Mach 8 runs with overpressures exceeding 7.5. In these latter runs, wide cavities are blown in the ambient medium. The ambient pressure gradually begins to rise after about 100 time units, with the excess energy being trapped on the grid despite the free outflow condition. The latter condition only inhibits the reflection of waves but does not ensure that gas flows out unless there is a pressure gradient to push it. Hence, the overpressure then falls, causing a collapse in the flow pattern size. We therefore doubled the physical sizes of the uniform and staggered grids in runs where we suspected this numerical effect was present, solving the issue.

The inner wall boundary condition does not apply in the aerodynamic context. There is no wall reflection of pressure waves that enhances oscillations in the first jet shock. Moreover, the motion of the propelled rocket through the atmosphere may aid stability by advecting surface waves downstream.

2.2 The scaling

The simulations are dimensionless and so can be scaled to any adiabatic inviscid gas. We set up our units in terms of the jet radius $R_{\text{jet}} = 1$ and the ambient sound speed, $c_{\text{amb}} = 1$. Hence, the unit of time is $R_{\text{jet}}/c_{\text{amb}} = 1$.

Taking the ambient density $\rho_{\text{amb}} = 1$ then fixes the ambient pressure,

$$p_{\text{amb}} = \frac{\rho_{\text{amb}} c_{\text{amb}}^2}{\gamma}. \quad (1)$$

This yields a pressure $p_{\text{amb}} = 1/\gamma = 0.6$ and internal energy per unit volume $u_{\text{amb}} = 0.9$ for the specific heat ratio of $\gamma = 5/3$ since

$$u_{\text{amb}} = \frac{p_{\text{amb}}}{\gamma - 1}. \quad (2)$$

Three parameters are specified to describe the jet at the nozzle: the Mach number, M , the pressure ratio $\kappa = p_{\text{jet}}/p_{\text{amb}}$, and the density ratio $\eta = \rho_{\text{jet}}/\rho_{\text{amb}}$. We fix the jet Mach number, M_{jet} , and then determine the jet speed as $v_{\text{jet}} = M c_{\text{jet}}$, where $c_{\text{jet}}^2 = \kappa/\eta$.

The simulations analysed here are listed in Table 2. Many other cases were explored including simulations where the Mach number was slowly increased in order to narrow down the transition between regular and Mach reflection.

Note that we ramp up the jet speed linearly from an initial value of zero up the constant v_{jet} . We take a default time to reach the final speed as $t_{\text{ramp}} = 10$ after trying numerous values and finding no significant further evolution to the flow pattern after ~ 90 time units up to the end of the runs at 200 time units.

Five physical properties are recorded to file at each of 1000 data dumps separated by 0.2 time units, allowing evolution over 200 time units. The parameters are the density, ρ , pressure, p , two velocity components, v_z (axial velocity) and v_r (radial velocity), and a mass-weighted jet tracer, χ .

3 OVERPRESSURED FLOW TYPES

In Fig. 1, we identify four flow types, all derived from Mach 2 simulations, where steep pressure gradients are displayed. In order to identify shock locations, we employed the pressure jumps in the

Table 2. Summary of simulations explicitly employed.

Figure number	Mach number	Pressure ratio, κ	Density ratio, η
1(a)	2	2	0.1
1(b)	2	4	0.1
1(c)	2	10	0.1
1(d)	2	16	0.1
2(upper)	2	1.1–16	0.1
2(lower)	2	1.1–16	10
3	4	2–12	0.1
4	2–7.5	2–24	10
5	1.1–8	8	10
6	4	2–12	0.1
7	8	2–12	0.1
8	1.1–8	8	10
9(left)	4	8	0.1
9(right)	6	8	0.1
10(left)	8	8	0.1
10(right)	8	8	10
11(upper)	8	2	0.1
11(lower)	8	16	0.1
12(upper)	4	4	0.1
12(lower)	4	14	0.1
13	4	14	0.1
14(upper)	4	2	0.1
14(middle)	6	2	0.1
14(lower)	8	2	0.1
15(upper)	4	2	0.1
15(middle)	6	2	0.1
15(lower)	8	2	0.1
16	8	6	10
17	8	2–16	10

radial and axial directions between neighbouring zones, δp_r and δp_z . After trials, we found that the quantity $(\delta p_r^2 + \delta p_z^2)/\sqrt{(p_r^2 + p_z^2)}$ generates a good representation of the shock patterns.

To track the interface, we used the jet tracer, $tr = 1$ and ambient medium value $tr = 0$ to calculate the zone differentials δtr_r and δtr_z . We then added a value of $0.8\sqrt{(tr_r^2 + tr_z^2)}$ to the above value for the shock jump to complete the flow patterns.

For a fixed Mach number, the flow pattern undergoes a major transition from regular reflection to Mach reflection at a critical overpressure, κ . This is shown in Fig. 2 for a Mach number of 2 and for relatively light jets (upper panel) and heavy jets (lower panel). The transition occurs at $\kappa_{\text{tran}} \sim 3.5$.

We have calculated the radius of the Mach shock disc at the end of each run. It should be noted that the flows are generally non-steady and the location as well as the radius can oscillate. We have also taken into account that the Mach disc is not vertical (i.e. radial). To account for this in the context of the simulations, we determine the radial distance of the pressure jump as a function of the axial distance, and then fit a parabolic function to determine the triple point where the shocks meet. In practice, this method works extremely well when we test against the values in the literature, as discussed below.

We find that the radius of the Mach disc corresponds to

$$R_{\text{MD}} = 0.6 \times (\kappa - 3.5)^{1/2} \quad (3)$$

for a Mach number of 2, for $\kappa > 3.5$. This fit, as shown by the dashed lines in Fig. 2, is based on that expected from previous studies as summarized by Franquet et al. (2015). However, their result was more general and was found for all low Mach number data.

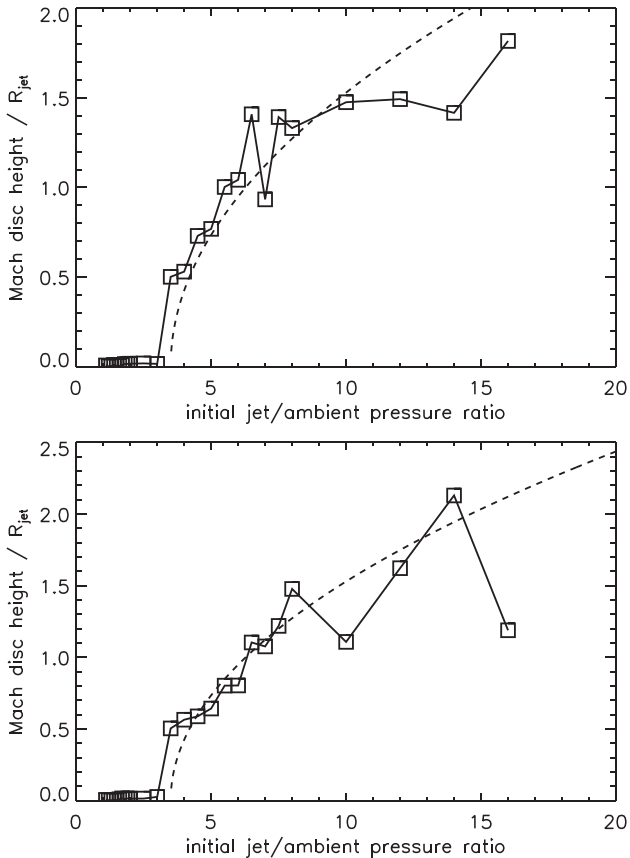


Figure 2. The radius of the Mach shock disc as a function of the overpressure κ for a jet with Mach number of 2, as measured after 200 time units. Upper panel is for a light jet with density of $\eta = 0.1$ of the ambient density and lower panel is for a relative jet with density of $\eta = 10$. The dashed line is the proposed fit from equation (3).

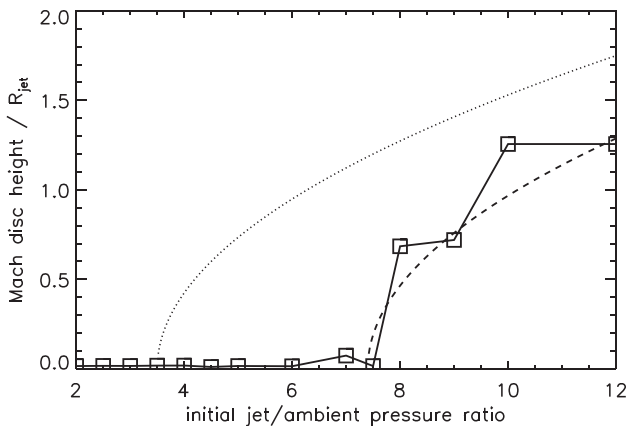


Figure 3. The radius of the Mach shock disc as a function of the overpressure κ for a jet with Mach number of 4, as measured after 200 time units. The panel is for a light jet with a density ratio of $\eta = 0.1$ of the ambient density. The dashed line is the proposed fit from equation (4), with the equation (3) dotted line shown for comparison.

To extend this to high Mach numbers, we first investigated the Mach 4 case for a large number of runs each with fixed overpressure. The results are displayed in Fig. 3. At higher Mach numbers, the transition from regular to Mach reflection occurs at

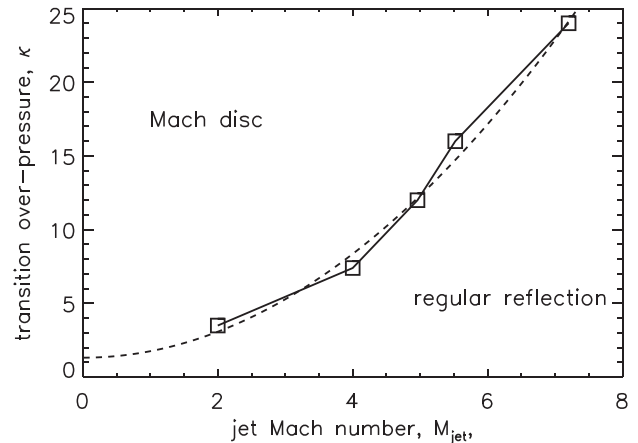


Figure 4. The transition from Mach shock discs to regular reflection in $M_{\text{jet}}-\kappa$ parameter space ($\eta = 10$). The dashed line is a semi-empirical fit based on the input parameters as discussed in the text.

higher overpressures. For Mach 4, as shown in Fig. 3, we find an approximate fit

$$R_{\text{MD}} = 0.6 \times (\kappa - 7.4)^{1/2}. \quad (4)$$

We thus deduce that there is indeed a Mach number dependence for the transition.

What causes the transition from regular to Mach reflection at a critical overpressure? In their classic work on supersonic flow, Courant & Friedrichs (1948) studied analytically the relationship between the angle of the oblique incident shock and the appearance of regular or triple-point reflection from a planar surface. For a specific heat ratio of 1.4, they found that the critical shock angle to the surface is $\sim 40^\circ$, with an overlap of a few degrees where both solutions are feasible. This implies that, for a given overpressure, a critical Mach number should exist above which the incident shock is reflected without the Mach stem and triple point.

We thus set up a number of simulations in which κ is fixed and the jet speed and Mach number are ramped up over 200 time units. Sharp transitions are found here typically identified over 0.6 of a time unit, although we take a heavy jet to expedite the runs. We find the transition Mach number, M_c to be

$$\text{for } \kappa = 12, M_c = 4.96,$$

$$\text{for } \kappa = 16, M_c = 5.52,$$

$$\text{for } \kappa = 24, M_c = 7.20.$$

Taken together, as shown in Fig. 4, this suggests that the transition occurs at

$$\kappa_{\text{tran}} \sim \kappa_M = 0.44 \left(M_{\text{jet}}^2 + \frac{2}{\gamma - 1} \right) \quad (5)$$

and the Mach disc radius is

$$R_{\text{MD}} = 0.6 \times (\kappa - \kappa_M)^{1/2}. \quad (6)$$

Here, we have defined $\kappa_M = c_{\text{jet}}^2 U^2$, where U is the Bernoulli constant. We thus include the enthalpy contribution to the nozzle power since this is significant at low Mach numbers. The Bernoulli constant for the flow, U (see equation A4 of SK22), is

$$U^2 = v_{\text{jet}}^2 + \frac{2\gamma}{\gamma - 1} \frac{p_{\text{jet}}}{\rho_{\text{jet}}}. \quad (7)$$

Remarkably, by including the enthalpy term, we recover the weak dependence on Mach number, consistent with the literature. It is clear

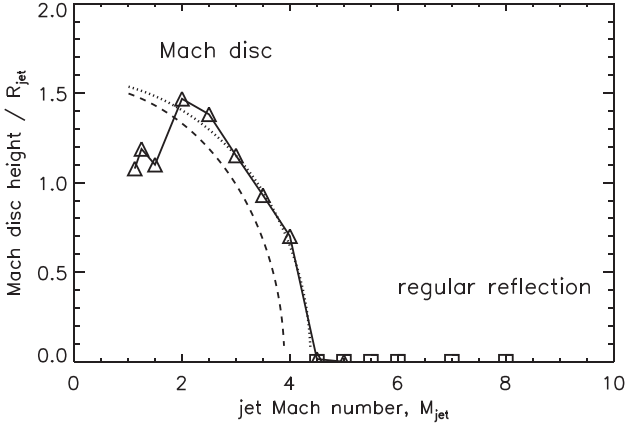


Figure 5. The height/radius of the stand-off Mach shock disc as a function of the Mach number for an overpressure of $\kappa = 8$ for a jet/ambient density ratio of $\eta = 10$, as measured after 200 time units. The symbols denote the total axial length of the uniform section of the grid that was doubled to $60R_{\text{jet}}$ for high Mach number runs (square symbols).

that the formula for the Mach shock disc should include the Mach number. However, for low Mach numbers, the dependence is weak.

This is also demonstrated in Fig. 5 where we present the quasi-steady final heights of the stand-off shocks for a wide range of Mach numbers. This set of simulations were all performed with a fixed overpressure of $\kappa = 8$. The form of the above formula (dashed line) is confirmed although a constant for $\kappa_M = 0.36$ (dotted line) is a much better fit.

We also note that for low Mach numbers, the size of the Mach disc is considerably smaller than that given by equation (6). Inspection of the images, shows that this corresponds to the downstream plume-type fully turbulent flow. Fully three-dimensional simulations are necessary to accurately model these flow patterns.

4 SHOCK SEPARATIONS

The distances of the shocks from the nozzle are calculated by locating the pressure jumps along the jet axis. For Mach 4 and Mach 8 jets, the locations are shown in Figs 6 and 7. The top panels show the linear displacements, while lower panels, with logarithmic units, allow for power-law fitting. The first shock, termed the stand-off shock, is found without ambiguity.

At low overpressures, we can determine the position of subsequent shocks in the regular pattern. However, oscillations cause weak pressure waves that we discount if adjacent to the strong shock.

In the case of regular reflection, we expect linear fits as found for Mach 2 jets by SK22. Linear fits to the stand-off shocks are shown by the dashed lines in the lower panels of Figs 6 and 7. The displayed analytical fit is derived from the equation

$$D_1 = \sqrt{(M_{\text{jet}}^2 - 1)\kappa^\beta} R_{\text{jet}}, \quad (8)$$

where we take $\beta = 1$. Hence for Mach 4, this yields $\log(D/R_{\text{jet}}) = 0.59 + \log \kappa$, while for Mach 8, this becomes $\log(D/R_{\text{jet}}) = 0.90 + \log \kappa$.

As shown below, the stand-off shock is approximately proportional to both the Mach number and overpressure in the regular reflection regime. Taking the lowest seven κ of the Mach 4 simulations, we find a least-squares fit of $\log(D/R_{\text{jet}}) = 0.67 + 0.90 \log \kappa$. Hence, the analytical result extends to high Mach numbers. Similarly, for Mach 8, we find a good fit: $\log(D/R_{\text{jet}}) = 0.91 + 0.90 \log \kappa$. However, this

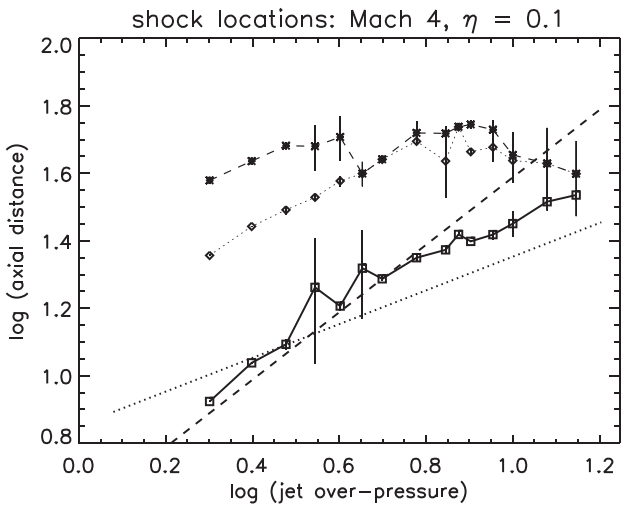
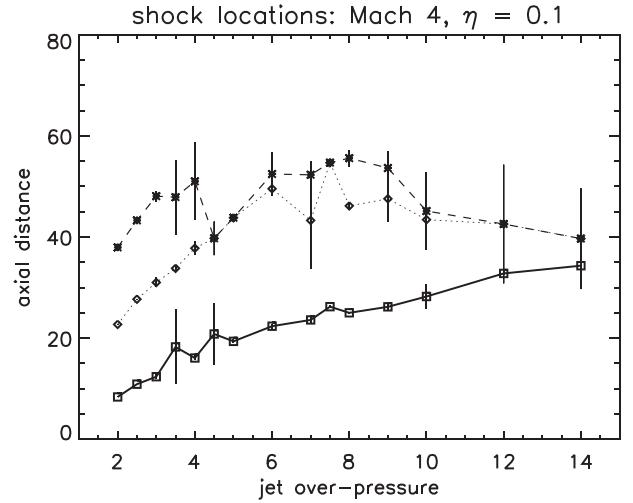


Figure 6. The distance of the first three shocks along the jet axis as a function of κ (upper panel) and $\log \kappa$ (lower panel) in units of the jet radius. For Mach 4, density ratio $\eta = 0.1$. The analytical power laws superimposed are those from the text with slope 1 (dotted line) and slope 0.5 (dashed line). The error bars were determined from a root-mean-square fit covering the final 5 time units in order to account for oscillations.

holds only for $\kappa < 8$ even though regular reflection occurs to much higher overpressures as shown in Fig. 4.

For Mach 2 jets, we found a distinct knee in the distribution of stand-off distances that corresponded to the transition between flow patterns. At the higher Mach numbers considered here, the knee is more akin to a bend.

Across and above the bend in the stand-off distance, corresponding to the Mach shock disc regime, we find approximate power-law fits: $\log(D/R_{\text{jet}}) = 0.86 + 0.60 \log \kappa$ for Mach 4 and $\log(D/R_{\text{jet}}) = 1.21 + 0.53 \log \kappa$ for Mach 8. These compare to the expected analytical fits shown as dotted lines in the lower panels of Figs 6 and 7,

$$D_1 = 1.38 \gamma^{1/2} \kappa^{1/2} M R_{\text{jet}}. \quad (9)$$

While the approximate square-root dependence is maintained at high Mach number, the stand-off distances are about a factor of ~ 1.25 larger.

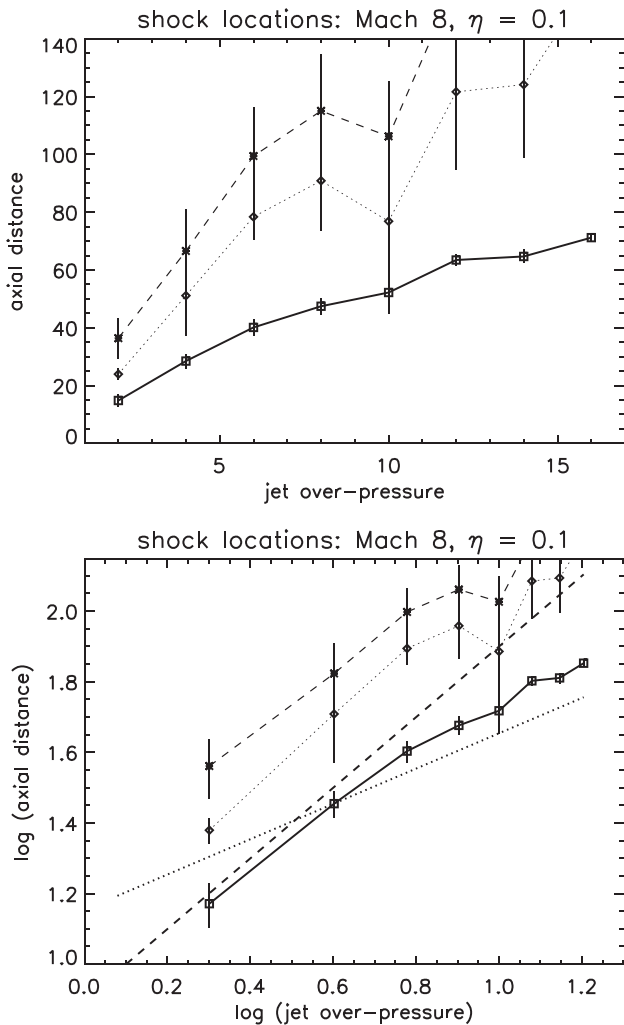


Figure 7. The distance of the first three shocks along the jet axis as a function of κ (upper panel) and $\log \kappa$ (lower panel) in units of the jet radius. For Mach 8, density ratio $\eta = 0.1$. The analytical power laws superimposed are those from the text with slope 1 (dotted line) and slope 0.5 (dashed line). The error bars were determined from a root-mean-square fit covering the final 5 time units in order to account for oscillations.

Finally, to test if the stand-off distance to the first shock remains proportional to the Mach number in these conditions, we ran simulations with a fixed overpressure. This is illustrated in Fig. 8. The dashed line corresponds to that of equation (9), and is consistent as expected in the (low Mach number) Mach disc regime.

At higher Mach numbers, in the regular reflection regime, a linear relationship is sustained as expected from that given by equation (8). This is shown as the dotted line in the lower panel. The simulated data reveals that the shock crosses the axis somewhat upstream of the predicted values. However, it is consistent with how the data also straddles between the two analytical models when the dependence on κ was investigated as shown in Figs 6 and 7.

5 FLOW FEATURES

In displaying snapshots of the flow it is recognized that the dimensions of the initial flow divergence and convergence are proportional to the Mach number. As we increase the Mach number at a fixed

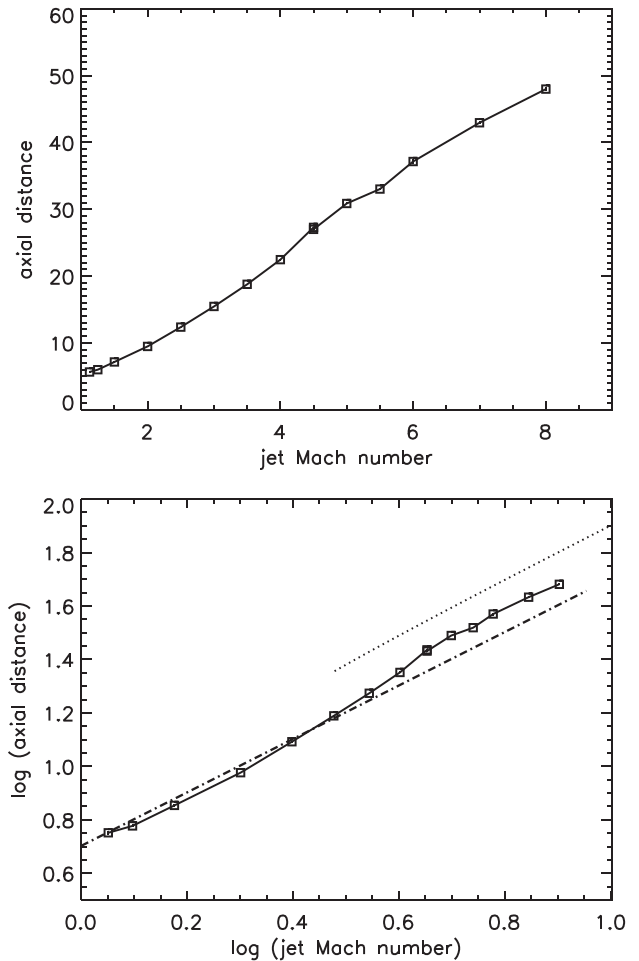


Figure 8. The stand-off distance of the first shock as a function of the Mach number for fixed overpressure of $\kappa = 8$ and for a jet/ambient density ratio of $\eta = 10$. Expressed on linear scales (upper panel) and logarithmic scales (lower panel), measured after 200 time units. The dotted and dashed lines correspond to the analytical formula of equations (8) and (9), respectively.

overpressure, the attained pattern is streamlined. Here, we display the physical parameters in equivalent square boxes by squeezing the numerical pixels along the x -axis by a factor of $2/M_{\text{jet}}$. We also manipulate the display of the jet tracer to emphasize the entrainment by using logarithmic values constrained to the range 0.001 to 1 where the jet mass carries a value of unity and the ambient medium zero.

Fig. 9 displays the physical parameters for Mach number of 4 and 6 for $\kappa = 8$ and $\eta = 0.1$. The displayed uniform axial section has been extended to 60 and 90 jet radii, respectively, and the time is 200 units.

For these low-density jets, much of the ambient material has been swept off the inner uniform grid by the initial bow shock as evidenced in the top-left panels. However, the jet interface remains well defined with the axial speed and tracer distributions in close correspondence. In addition, the pressure on the uniform grid, as shown in the lower-right panels, has had ample time to return to the initial ambient pressure as controlled by the large-scale ambient reservoir.

The axial speeds, corresponding to the low jet density, are high. A particular feature in the top-right panels, is the low speed spine that occurs after the Mach shock disc. The spine is separated from the fast sheath by a slip line.

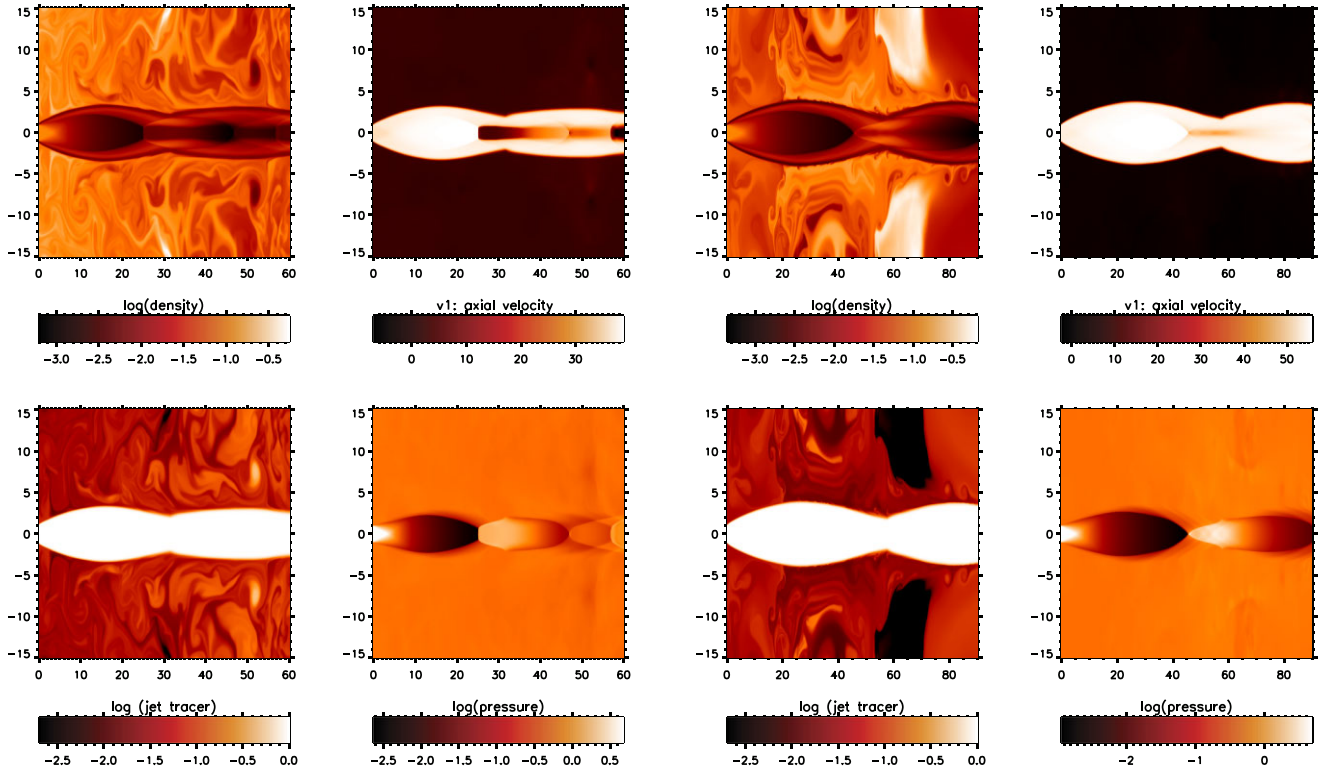


Figure 9. The distributions of physical parameters for Mach 4 (left panels) and Mach 6 (right panels) jets with overpressure of $\kappa = 8$ and density ratio of $\eta = 0.1$. The time $t = 200$ corresponds to the end of the run at $t = 200R_{\text{jet}}/c_{\text{amb}}$. The length-scale is in units of the jet radius with the x -axis units reduced so that the flow fits into a square panel. For both jets: upper-left panel: density, upper-right panel: axial velocity component, lower-left: tracer for jet gas, and lower-right: pressure.

The tracer panels at the lower left show significant structure. The material originating from the jet that is seen in the ambient medium has been deposited there during the initial outflow stage. Jet material is diverted into a cocoon where some of it remains trapped in vortices in which the pressure is slightly lower.

Fig. 10 displays the physical parameters for a Mach number of 8 with $\kappa = 8$. For a light jet with $\eta = 0.1$, on the left, we display the complete uniform cross-cuts that have been doubled to prevent anomalous effects caused by the free-outflow boundary conditions.

The heavy jet equivalent is shown in the right panels of Fig. 10 for $\eta = 10$. The standard grid is sufficient in this case because a heavy jet penetrates through the ambient medium creating a narrow cavity.

An interesting difference between the light and heavy jets is seen in the lower-left tracer panels. The heavy jet leaves behind several substantial clumps of original undisturbed ambient gas on a scale of $5R_{\text{jet}}$. Although heavy jets are efficient at drilling through ambient gas, the jet material that gets entrained has a low speed. These clumps have reached equilibrium with the ambient material, being only visible as a jet tracer.

These snapshots do not reveal the entire story. For that, we need to study the movies or, as displayed in Fig. 11, analyse the space-time diagrams. These diagrams show the pressure along the jet axis for each of the 1000 data files. These generally indicate whether or not the flow has evolved into a steady flow pattern. The initial advancing bow shock and undisturbed ambient medium occupy the lower-right region on these diagrams.

Oscillations are present in all the simulations shown in Figs 11 and 12. Fig. 11 shows the multiple shocks associated with regular reflection. Both panels display light Mach 8 jets with the only difference being the overpressure.

The variations are better described as stochastic with a time-scale of up to 2–5 time units. The pressure variations can propagate both downstream and upstream, suggesting that positive feedback is at play but with no resonant or coherent amplification. It should be remarked that the transition between flow patterns is not fixed and the variations can lead to Mach shock discs temporarily appearing or disappearing.

The lower panel of Fig. 12 illustrates the structure of Mach reflection on a space-time diagram. The high overpressure $\kappa = 14$ yields a distinct high-pressure region downstream of the stand-off disc, as opposed to the regular well-spaced shocks for $\kappa = 4$ (upper panel).

We find examples of all flow patterns at high Mach numbers. For example, the Mach 4 jet with $\kappa = 14$ discussed above does not have a full plume flow but does correspond to a sheath flow as shown in Fig. 1. This is clarified in Fig. 13 where the pressure panel confirms the high-pressure region downstream of the Mach disc. However, the top-left panel shows that the density here is extremely low despite the shock compression.

6 POWER AND ENERGY

A channel with a repeating divergent–convergent structure occurs in the regular reflection regime. Therefore, the flux of the components that contribute to the energy flow across the grid will also oscillate for regular reflection. This is confirmed in Fig. 14 for a range of high Mach numbers with the overpressure fixed at the low value of 2. The census is taken at the end of each run. The integrated power through each cross-section normal to the jet axis is shown, with the power unit in terms of $\rho_{\text{amb}}c_{\text{amb}}^3R_{\text{jet}}^2$.

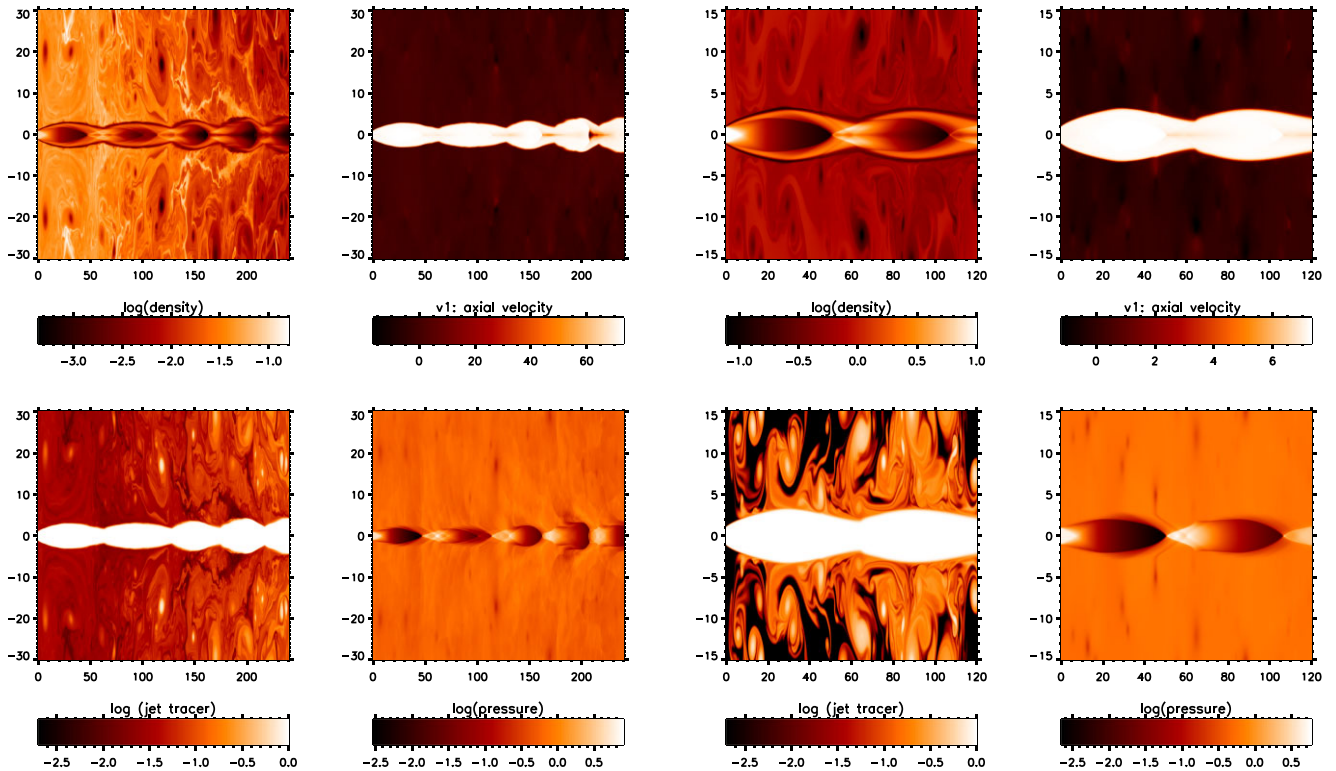


Figure 10. The distributions of physical parameters for Mach 8 jets. The left panels display a light jet with $\eta = 0.1$ that required an extended grid to ensure that the ambient pressure could freely evolve. The right panels are for a heavy jet with $\eta = 10$ and are on a standard grid. All panels are for an overpressure of $\kappa = 8$ and time $t = 200$. The length-scale is in units of the jet radius, with the x -axis units reduced so that the flow fits into a square panel. For both jets: upper-left panel: density, upper-right panel: axial velocity component, lower-left: tracer for jet gas, and lower-right: pressure.

The kinetic energy flux in the jet (solid lines) varies smoothly, with the total jet energy (dotted lines) approximately constant, the fall being under 2 per cent. This is of course due to the adiabatic equation of state: if the flow channel reaches a perfectly steady state, there is no path for energy loss.

A striking feature at these high Mach numbers is the spatial variation in the flux within the ambient medium. A large difference between the total jet power and the power within the ambient medium is found. As stated above, a steady flow is almost attained within the jet, as evidenced by the dotted lines. In contrast, the ambient medium contains large-scale vortices that are long-lived, as shown by the large variations in the dot-dashed lines in Fig. 14. In the panels, this is represented by the difference between the total power and the total (exclusively) jet power.

The variations in the ambient medium are associated with subsonic motions of the relatively dense gas, as previously heated gas circulates. This behaviour was not found in the equivalent low Mach number case. It can be explained by inspecting the space-time diagrams. Whereas a stationary shock pattern was found in the Mach 2 case, distinct oscillations dominate all the shock locations at high Mach numbers, as illustrated here in Fig. 11. These oscillations are responsible for stirring and advecting adjacent ambient gas. The energy transfer is, however, typically just a few per cent of the total jet power, varying across the grid on the scale of the distance between regular reflections.

To elaborate, the total kinetic power through a circular cross-section at an axial distance, z , is

$$P_{\text{total}}(z) = \int \frac{1}{2} \rho v^2 v_z dA, \quad (10)$$

where v is the speed, A is the normal area, and v_z is the axial component of velocity. The jet kinetic power is defined as

$$P_{\text{jet}}(z) = \int \frac{1}{2} \chi \rho v^2 v_z dA, \quad (11)$$

where χ is the tracer for the material originating from the nozzle.

The total power includes the enthalpy (thermal and $p dV$). It is expressed by replacing v in the above equations with the Bernoulli constant U , where

$$U^2 = v_{\text{jet}}^2 + \frac{2\gamma}{\gamma - 1} \frac{p_{\text{jet}}}{\rho_{\text{jet}}}. \quad (12)$$

The transfer of energy off the grid as a function of time is presented in Fig. 15. Displayed is the rate of energy crossing an imaginary cylindrical surface at a radius and axial length of 90 per cent of the uniform grid. Hence, the lateral power is associated with the escape through the tube, while the jet power components are given by the fluxes through the end-cap of the cylinder.

In detail, to calculate the balance of power, we choose a cylindrical surface of radial and axial lengths of 90 per cent of the uniform section. The kinetic and total jet powers are then determined as a function of time at this axial distance using the above formulae. The lateral powers are similarly calculated with the axial speed replaced by the radial speed and then integrating. Hence, a positive power implies a lateral outflow of energy.

For the simulations shown, it takes ~ 30 time units before the jet bow shock advances to the cap. Hence, the high peak represents the jet drilling through the (virtual) cap which then continues through the simulation.

The lateral power rapidly increases soon after the outset as the wings of the bow shock cross the inner tubular surface of the grid

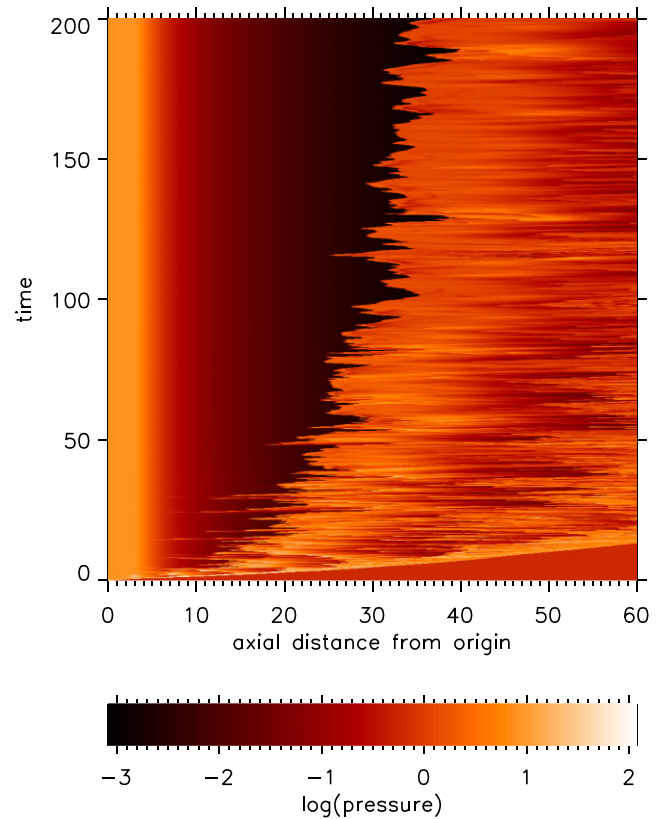
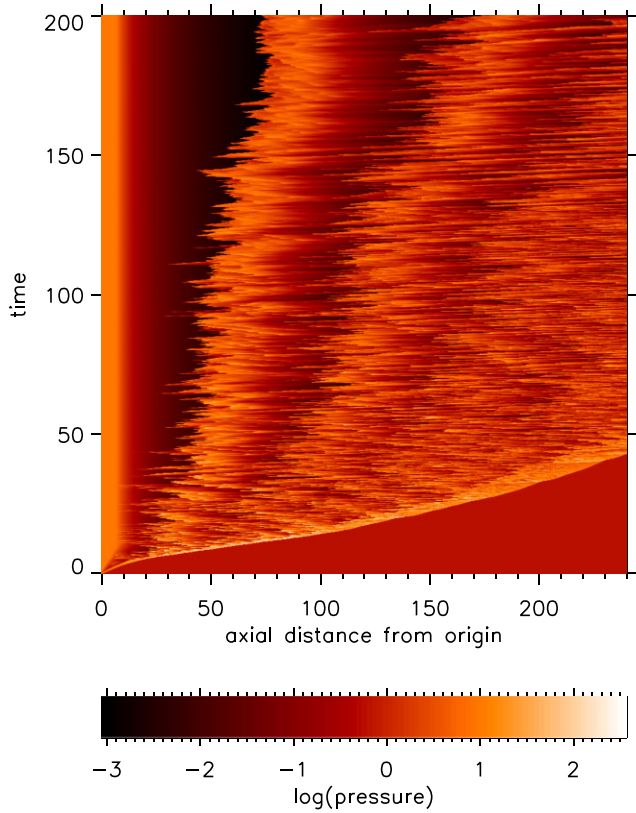
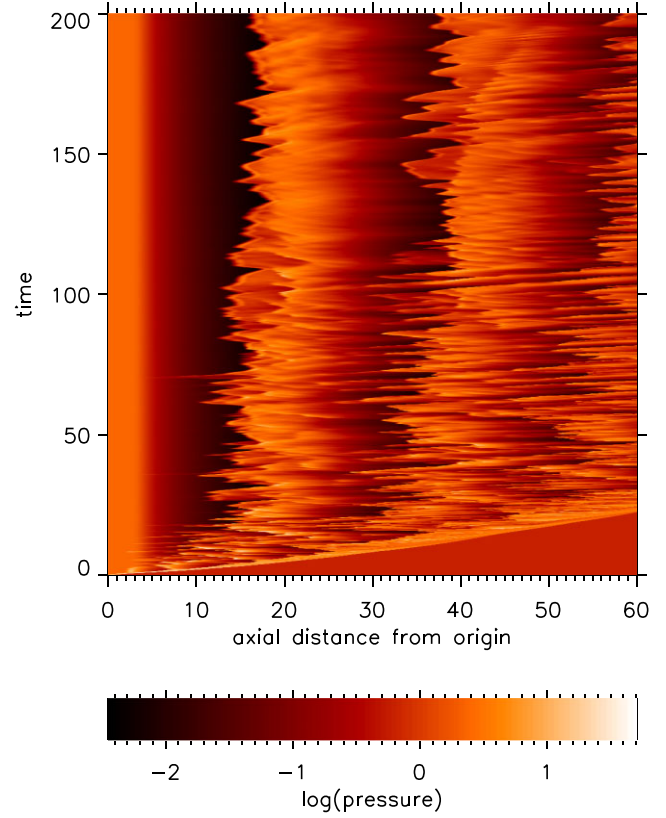
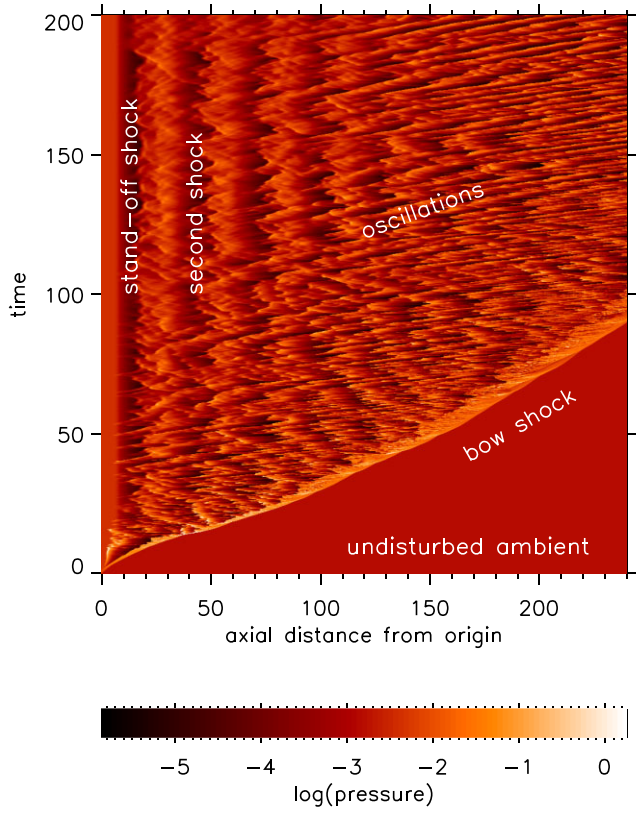


Figure 11. Space–time diagrams for Mach 8 jets, with $\kappa = 2$ (upper panel) and $\kappa = 16$ (lower panel) and initial density ratio $\eta = 0.1$. The distribution of the pressure along the jet axis (x -axis) is shown as a function of the time (y -axis). Length-scale is in units of the jet radius.

Figure 12. Space–time diagrams for Mach 4 jets with density ratio of $\eta = 0.1$ and initial overpressures of $\kappa = 4$ (upper panel) and $\kappa = 14$ (lower panel). The distribution of the pressure along the jet axis (x -axis) is shown as a function of the time (y -axis). Length-scale is in units of the jet radius.

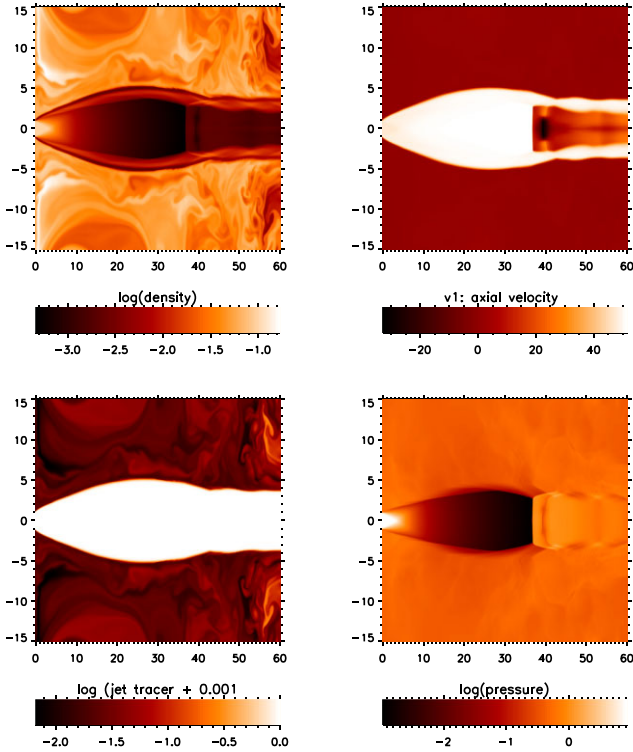


Figure 13. The distributions of physical parameters for a sheath-type Mach disc flow pattern found for a Mach 4 jet with $\kappa = 14$ and density ratio of $\eta = 0.1$. The time $t = 200$ corresponds to the end of the run at $t = 200R_{\text{jet}}/c_{\text{amb}}$. The length-scale is in units of the jet radius with the x -axis units reduced so that the flow fits into a square panel. Upper-left panel: density, upper-right panel: axial velocity component, lower-left: tracer for jet gas, and lower-right: pressure.

cylinder. The red dotted lines indicate that this energy is being convected sideways in the form of hot thermally heated gas. The bow shock itself does also transfer some kinetic power as indicated by the green dot-dashed lines. This is consistent with propagating jet simulations which conclude that ~ 70 per cent of jet energy is transmitted into the surroundings in the form of hot slow-moving gas (O'Neill & Jones 2010; Donohoe & Smith 2016).

As the flow pattern settles down, the net lateral power decreases down to small values of a few per cent. The lateral energy flow is usually positive once settled with minor negative excursions. This contrasts with the Mach 2 case (see SK22) where a negative lateral energy flux is the norm. Thus, at low Mach numbers there is a tendency to advect gas along the axis but this effect is largely absent at higher Mach numbers.

In summary, the injection of steady overpressured jets may contribute to noise and sound wave generation through the sharp irregular oscillations, termed screeching. However, in the near-field, they are not sufficiently significant to alter the medium so as to regulate star and galaxy formation.

7 DISCUSSION

The eventual aim is to attribute an observed jet brightness distribution to the underlying physical parameters. In this work, we locate the shock fronts but to not attempt to convert these into simulated images. We also note that we are limited here to adiabatic hydrodynamics

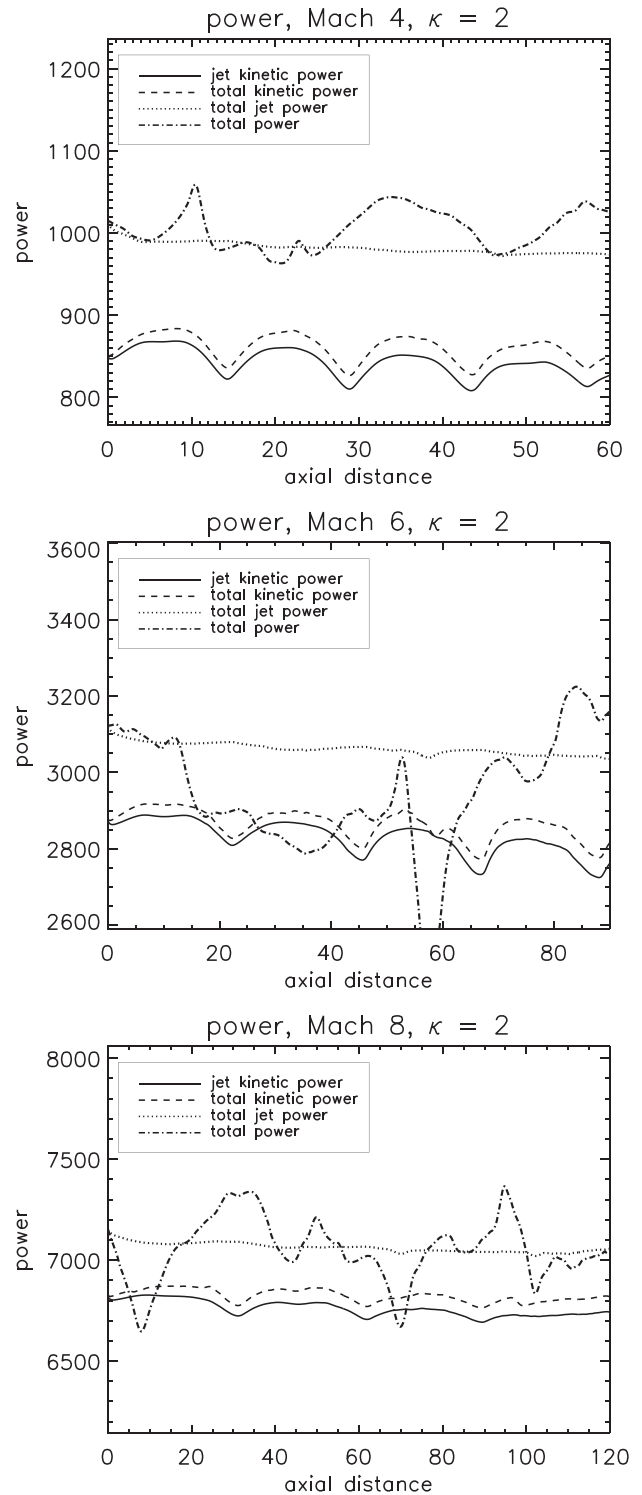


Figure 14. The integrated axial power across each entire circular cross-section as a function of axial distance from the orifice boundary, at the end of the simulations. Density ratio $\eta = 0.1$ for Mach 4 (top), 6 (middle), and 8 (lower panel) jets.

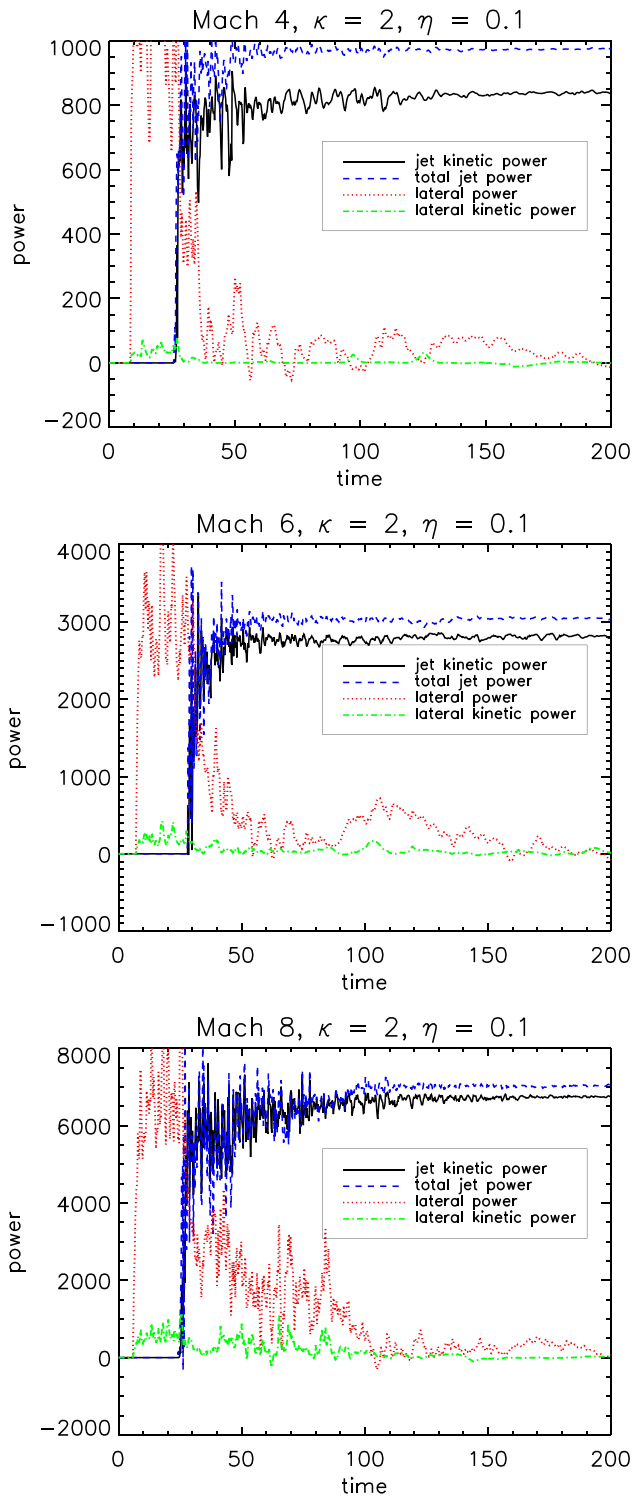


Figure 15. Evolution of the lateral and forward escape of energy for low density ratio jets ($\eta = 0.1$). The energy flux is out of a cylindrical surface, drawn with radius 180 zones and axial length of $360 \times M_{\text{jet}}$ zones. Initially, the jet enters the grid and it takes ~ 30 time units to cross to the cylinder cap that is at 90 percent of the uniform grid length. The power is expressed in simulation units, $\rho_{\text{amb}} c_{\text{amb}}^3 R_{\text{jet}}$. The panel titles provide the pressure ratio κ and Mach numbers.

and therefore any emitted radiation should not be accompanied with significant cooling that would invalidate energy conservation.

The most distinguishing features are the patterns associated with Mach discs and regular reflection. The dividing line between these depends on the Mach number and overpressure. A rule of thumb is that a Mach disc is present for $\kappa > 0.5M_{\text{jet}}^2$. The adiabatic index will have some influence that has not been investigated here.

This result on the appearance of Mach discs extends previous laboratory and computational experiments. It was previously concluded that Mach discs are formed when the total or stagnation overpressure $\kappa_s > 4$, although it is commonly assumed that the nozzle speed is sonic ($M_{\text{jet}} = 1$) (Menon & Skews 2010; Hamzehloo & Aleiferis 2016).

These results were confirmed as a prelude to the first supersonic jet simulations by Norman et al. (1982). They took a κ of 2.75, $M_{\text{jet}} = 1$ and $\gamma = 7/5$ to compare with earlier laboratory data finding excellent agreement.

The sonic nozzle is the subject of many investigations into the escape of gas from a large reservoir through a small hole. The gas is then taken to be sonic at the exit, and assumed to correspond to the minimum cross-sectional area (Rahantamialisoa et al. 2022; Lei et al. 2023). The quantity of interest is often the energy of the injected compressed gas that corresponds to the stagnation pressure, which is approximately double that of the exit pressure following the adiabatic expansion. Moreover, extremely high overpressures are usually relevant for the motivation of the research, such as hydrogen fuel injection engines (Hamzehloo & Aleiferis 2016). The studies focus on the nature of the vortices that make up the turbulent plume. In these studies, a virtual nozzle substitutes for the actual orifice at the point where the plume begins.

In contrast, we do not assume a sonic nozzle, and so we need to introduce the Mach number as a further independent variable. Moreover, we have a special interest in low overpressures since astrophysical jets are often efficient conveyors of energy to large distances rather than forming a plume.

How can a supersonic gas jet, that has been confined by and collimated close to the source, become out of pressure balance with its surroundings? If we consider the jet to form within a dense gravitational bound core supported by thermal pressure, a quite sharp pressure gradient could ensue. Alternatively, a transient event may release a powerful jet that is far out of pressure equilibrium. Hence, the jet itself may be in a state of free expansion. Such jets will be the subject of subsequent work in which we can make a direct comparison.

On the other hand, jets that are supplied by reservoirs below the surface of Solar system bodies would indeed emerge with a high overpressure. Furthermore, the nozzle may be shaped and smoothed over time, generating a tunnel with hard polished walls from which a high Mach number jet exits.

The jet density may not have a large influence on the attained shock pattern but is crucial to the oscillations and variations superimposed. Heavy jets maintain their flow pattern with longer oscillations of smaller amplitude. This is illustrated in Fig. 16.

In addition, for heavy jets, the stand-off distance very closely follows that of the light jets, as illustrated in Fig. 17. The analytical guidelines are those shown in Fig. 7, where the data clearly follow the same trend but with less variation.

Proper motions in astrophysical jets are commonly in the general direction of the axis with an advancing speed consistent with that of the gas motion as estimated from radial velocities and projection angles (e.g. Potravnov et al. 2022).

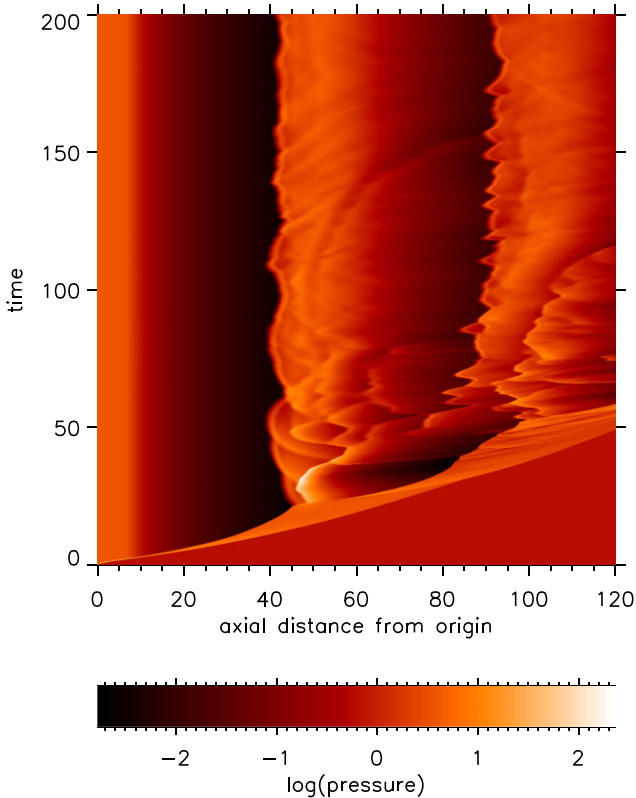


Figure 16. Space–time diagram for a heavy Mach 8 jet with initial overpressure of $\kappa = 6$. Note the oscillations in the position of the stand-off shock are of low amplitude and occur on a time-scale of ~ 10 time units. The distribution of the pressure along the jet axis (x -axis) is shown as a function of the time (y -axis) for a density ratio of $\eta = 10$. Length-scale is in units of the jet radius.

However, there are examples where stationary (Agudo et al. 2012; Snios et al. 2019) and even apparent contraction have been detected (Kellermann et al. 2004). In the case of 3C78 (Oriente & Dallacasa 2010; Roychowdhury 2022), speeds are relativistic.

Shock diamonds were invoked by Ustamujic et al. (2016) to interpret a stationary X-ray knot in the HH154 protostellar jet discovered by Favata et al. (2006). Using a similar simulation setup, Ustamujic et al. (2018) considered pulsed jets with an external magnetic field to specifically interpret HH154.

We note that rapidly receding shocks are predicted here as shown by the horizontal spikes in the space–time diagrams. The spikes typically convert to speeds of $5\text{--}20c_{\text{amb}}$, while jet speeds are $30\text{--}60c_{\text{amb}}$. Hence, more repositioning is expected. We suspect that a stationary shock is indeed involved, but a second propagating shock has impacted it, generating a strong reflected shock. We intend to explore interactions in an upcoming work.

Stationary emission structures, consistent with first stand-off shocks, are being found within resolved nearby extragalactic jets. The M87 knot A was proposed by Eichler & Smith (1983) to be a Mach shock disc, based on the apparent normal shock front. Since then, detailed observations suggest complex components and proper motions involving a helical magnetic field (e.g. Avachat et al. 2016). The Seyfert 1H 0323+342 jet also contains a stationary recollimation shock (Hada et al. 2018). The jet narrows at the recollimation shock before the jet opens up conically, further downstream. This could correspond to a plume-type flow as shown in Fig. 1, although the narrowing would suggest that the Mach disc does not traverse the entire jet, as in panel (c).

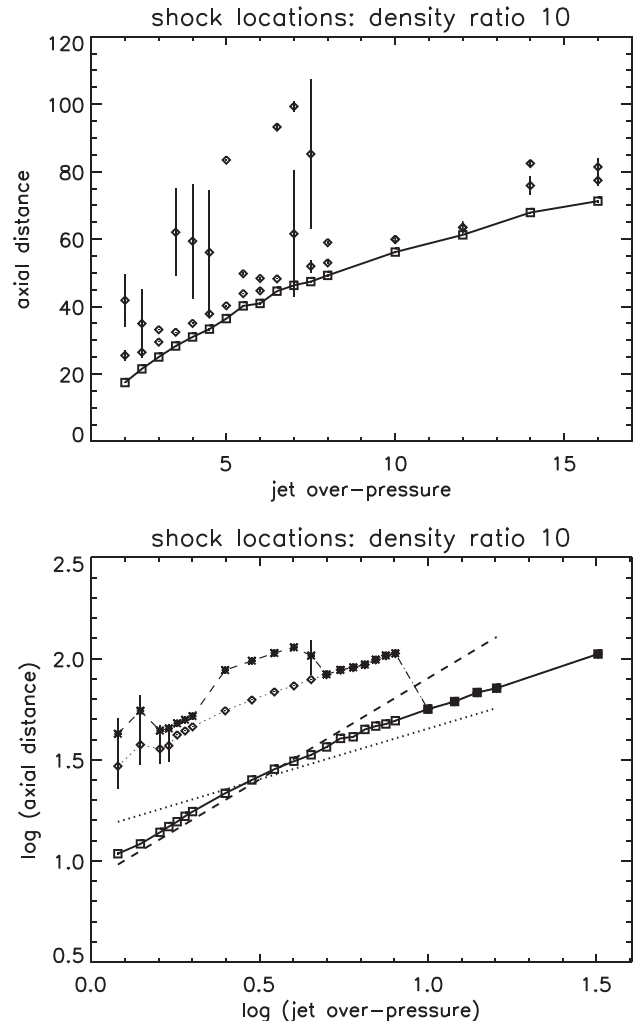


Figure 17. The distance of the first three shocks along the jet axis as a function of κ (upper panel) and $\log \kappa$ (lower panel) in units of the jet radius. For Mach 8, density ratio $\eta = 10$. The analytical power laws superimposed are those from the text with slope 1 (dotted line) and slope 0.5 (dashed line). The error bars were determined from a root-mean-square fit covering the final 5 time units in order to account for oscillations.

8 CONCLUSIONS

We have performed a systematic study of supersonic hydrodynamic jets with a range of Mach numbers. We focus on the near-field of jets with a high pressure relative to the ambient medium. The near-field flow settles into shock patterns with two extremes.

At low overpressures and high Mach numbers, a diamond shock pattern occurs in which a series of regularly spaced conical shock fronts is generated. At the other extreme, of high overpressures and low Mach numbers, oblique shocks do not cross the axis but are intercepted by a near-perpendicular disc-shaped shock front that reflects the incident shock at a connecting triple point. The transition is expressed by equation (3) and displayed graphically in Fig. 4.

The two major results required a large number of simulations to establish. These are the distance of the stand-off shock from the nozzle and the radius of the Mach shock disc. Both depend on the Mach number and the overpressure, and extend existing results found for low Mach number flows.

We find that the stand-off distance splits into two, corresponding to the flow pattern, as was found for the Mach 2 case. At low overpressures, the distance to the first shock along the axis occurs at approximately $\sqrt{(M_{\text{jet}}^2 - 1)\kappa} R_{\text{jet}}$.

At high overpressures, there is a gradual transition in the stand-off distance to a $\sqrt{\kappa}$ behaviour. This would be expected from the Mach 2 case that followed expectations based on ram pressure arguments. At high Mach numbers, however, the stand-off distance is approximately 1.25 times further from the nozzle.

Note that the Mach shock disc occurs at extremely large distances downstream for the parameters chosen in this paper, typically $30\text{--}60R_{\text{jet}}$. Thus, the shock location becomes very sensitive to the numerical resolution and nozzle set-up.

The dependence on the specific heat ratio (i.e. the adiabatic index) has been included via analytical expectations but has not been tested here where we fix $\gamma = 5/3$.

It is imperative to understand when Mach shock discs may occur in hypersonic jets since these are strong shocks with distinguishing fronts that would be recognizable. We have discussed observations in which stationary emission knots have been detected. In general, we require the new generation of telescopes to adequately resolve across the jets.

In astrophysics, we are often faced with high Mach number flows that are in the hypersonic regime. However, existing laboratory and numerical experiments have explored low Mach number jets, usually with $M < 3$. To date, studies of hypersonic jets have not systematically explored potential flow patterns but have provided illustrative examples to demonstrate the structures that magnetic fields, relativity, and cooling can introduce.

We have thus here taken a step backwards to first explore adiabatic flows with a wide range of Mach numbers and overpressures. We establish empirical laws that have plausible physical interpretations. However, it is important to note that most environments will greatly differ from those taken here: jet shear, jet spray, ambient pressure gradients, and ambient inhomogeneities will modify these results.

The degree of transport of energy into the ambient medium has consequences for diverse applications. It determines the noise level of rocket exhausts, the ability for jet feedback to support gas within galaxies, and protostellar clumps. We find that for high Mach number flows the net flow of energy transported both axially and laterally is low. The oscillations in jet structure do not cause as much advection as for the Mach 2 case. However, imposed pulsations and bursts within the jet could well alter this conclusion based on constant input conditions and will be the subject of a following work.

There is growing observational evidence that outflows from active galactic nuclei are capable of substantially altering the galactic, circumgalactic, and intergalactic media (Rawlings & Jarvis 2004; Venturi et al. 2021; Hillel et al. 2022; Krause 2023). Models generally support this, although large fractions of jet energy can only be deposited through the initial bow shock and radio lobes. Once the main jets have propagated beyond the near-field, the oscillations found here can only provide a modest input of energy, which can be analogously referred to as noise. However, we have here only established the fundamental physical properties and further work is necessary to model jet and ambient medium scenarios more relevant to extragalactic jets.

DATA AVAILABILITY

No new observational data were generated or analysed in support of this research. Simulation source files are available on request. The

data underlying this article will be shared on reasonable request to the corresponding author.

REFERENCES

- Agudo I., Gómez J. L., Casadio C., Cawthorne T. V., Roca-Sogorb M., 2012, *ApJ*, 752, 92
- Avachat S. S., Perlman E. S., Adams S. C., Cara M., Owen F., Sparks W. B., Georganopoulos M., 2016, *ApJ*, 832, 3
- Bally J., 2007, *Ap&SS*, 311, 15
- Belan M., Massaglia S., Tordella D., Mirzaei M., de Ponte S., 2013, *A&A*, 554, A99
- Belan M., Tordella D., De Ponte S., Mignone A., Massaglia S., 2014, *New J. Phys.*, 16, 085002
- Blackman E. G., Lebedev S. V., 2022, *New Astron. Rev.*, 95, 101661
- Courant R., Friedrichs K. O., 1948, *Supersonic Flow and Shock Waves*. Interscience Publishers, New York
- Donohoe J., Smith M. D., 2016, *MNRAS*, 458, 558
- Eichler D., Smith M., 1983, *Nature*, 303, 779
- Favata F., Bonito R., Micela G., Fridlund M., Orlando S., Sciortino S., Peres G., 2006, *A&A*, 450, L17
- Franquet E., Perrier V., Gibout S., Bruel P., 2015, *Prog. Aerosp. Sci.*, 77, 25
- Hada K. et al., 2018, *ApJ*, 860, 141
- Hamzehloo A., Aleiferis P., 2016, *Int. J. Hydrogen Energy*, 41, 6544
- Hillel S., Schreier R., Soker N., 2022, *MNRAS*, 514, 3212
- Kellermann K. I. et al., 2004, *ApJ*, 609, 539
- Krause M. G. H., 2023, *Galaxies*, 11, 29
- Lei Y., Wang X., Zhou D., Qiu T., Jin W., Qin C., Zhou D., 2023, *Heliyon*, 9, e13645
- Martí J.-M., 2019, *Galaxies*, 7, 24
- Menon N., Skews B. W., 2010, *Shock Waves*, 20, 175
- Mignone A., Bodo G., Massaglia S., Matsakos T., Tesileanu O., Zanni C., Ferrari A., 2007, *ApJS*, 170, 228
- Norman M. L., Winkler K.-H. A., Smarr L., Smith M. D., 1982, *A&A*, 113, 285
- O'Neill S. M., Jones T. W., 2010, *ApJ*, 710, 180
- Orienti M., Dallacasa D., 2010, *MNRAS*, 406, 529
- Perucho M., Martí J. M., 2007, *MNRAS*, 382, 526
- Potravnov I. S., Khovritchev M. Y., Artemenko S. A., Shakhovskoy D. N., 2022, *MNRAS*, 516, 5863
- Rahantamialisoa F. N. Z., Zembi J., Miliuzzi A., Sahranavardfard N., Battistoni M., 2022, *J. Phys.: Conf. Ser.*, 2385, 012051
- Rawlings S., Jarvis M. J., 2004, *MNRAS*, 355, L9
- Roychowdhury A., 2022, 44th COSPAR Scientific Assembly, Athens, Greece. 44, 2061, available at: <https://ui.adsabs.harvard.edu/abs/2022cosp..44.2061R/abstract>
- Schneider P. C., Günther H. M., Schmitt J. H. M. M., 2011, *A&A*, 530, A123
- Smith M. D., 2012, *Astrophysical Jets and Beams*. Cambridge Univ. Press, Cambridge
- Smith M. D., Donohoe J., 2019, *MNRAS*, 490, 1363
- Smith M. D., Donohoe J., 2021, *MNRAS*, 502, 423
- Smith M. D., Keogh T. L. R., 2022, *MNRAS*, 516, 2757 (SK22)
- Snios B. et al., 2019, *ApJ*, 871, 248
- Toro E. F., Spruce M., Speares W., 1994, *Shock Waves*, 4, 25
- Ustamujic S., Orlando S., Bonito R., Miceli M., Gómez de Castro A. I., López-Santiago J., 2016, *A&A*, 596, A99
- Ustamujic S., Orlando S., Bonito R., Miceli M., Gómez de Castro A. I., 2018, *A&A*, 615, A124
- Velović V. et al., 2022, *MNRAS*, 516, 1865
- Venturi G. et al., 2021, *A&A*, 648, A17
- White M. C., McGregor P. J., Bicknell G. V., Salmeron R., Beck T. L., 2014, *MNRAS*, 441, 1681
- Yelle R. V., Soderblom L. A., Jokipii J. R., 2004, *Icarus*, 167, 30

This paper has been typeset from a \LaTeX file prepared by the author.

© 2023 The Author(s).

Published by Oxford University Press on behalf of Royal Astronomical Society. This is an Open Access article distributed under the terms of the Creative Commons Attribution License (<http://creativecommons.org/licenses/by/4.0/>), which permits unrestricted reuse, distribution, and reproduction in any medium, provided the original work is properly cited.